Label-Free High-Density Mapping Reveals Sustained Reentrant Activity in iPSC-Derived Atrial Cardiomyocytes from Brugada Syndrome Patients

Wener Li[1]*, Irem Congur[1], Björn Binnewerg[1], Mario Schubert[1], Xiaojing Luo[1], Sabine Schmidt[2], Yuliya Dzekhtsiarova[1], Wenjing Tao[1], Martin Bulst[3], Sebastian Wegner[3], Heinz-Georg Jahnke[2], Kaomei Guan[1]*

[1]Institute of Pharmacology and Toxicology, Carl Gustav Carus Medical Faculty, Technische Universität Dresden, Fetscherstraße 74, 01307 Dresden, Germany

[2]Centre for Biotechnology and Biomedicine, Biochemical Cell Technology, Leipzig University, Deutscher Platz 5, 04103 Leipzig, Germany

[3]Sciospec Scientific Instruments GmbH, Leipziger Str. 43b, 04828, Bennewitz, Germany

* Corresponding author. Email: kaomei.guan@tu-dresden.de; wener.li@tu-dresden.de

Keywords: high-density microelectrode array, re-entry, Brugada syndrome, atrial fibrillation, induced pluripotent stem cell-derived atrial cardiomyocytes

ABSTRACT

Atrial fibrillation (AF) is unexpectedly prevalent in Brugada syndrome (BrS), yet the mechanisms linking *SCN5A* loss-of-function to atrial instability remain elusive. Here, we combined patient-specific induced pluripotent stem cell-derived atrial cardiomyocytes with label-free high-density microelectrode array (HD-MEA) mapping. We show that *SCN5A* haploinsufficiency creates an arrhythmogenic substrate driven by the concomitant loss of excitability and heterogeneous Cx40 remodeling. This specific architecture renders mutant atrial syncytia highly susceptible to sustained, high-frequency spontaneous micro-reentry, a reentry-in-a-chip phenotype not recapitulated by pharmacological sodium-channel blockade in controls. Notably, genotype-negative BrS lines lacked spontaneous instability, exhibiting only inducible arrhythmia. Pharmacological profiling demonstrated that rhythm-control agents terminated reentry, whereas rate-control agents solely slowed rotation. This study defines the first human *in vitro* model of spontaneous atrial reentry, distinguishing primary mutation-driven defects from secondary clinical remodeling and providing a precision platform for anti-arrhythmic drug discovery.

TEASER

High-density mapping in patient-derived heart cells reveals how sodium channel deficiency and gap junction remodeling drive spontaneous atrial reentry.

INTRODUCTION

Atrial fibrillation (AF) is the most common sustained cardiac arrhythmia and a major cause of stroke, heart failure, and cardiovascular morbidity worldwide (*1*). AF is unexpectedly prevalent in patients with Brugada syndrome (BrS), despite BrS being classically viewed as a ventricular conduction disorder. Continuous rhythm monitoring has revealed a substantial burden of atrial tachyarrhythmias even in young BrS patients, indicating compromised atrial conduction reserve (*2-4*). Loss-of-function mutations in *SCN5A*, encoding the cardiac sodium channel $Na_V1.5$, represent the most common genetic cause of BrS (*5*). However, a human experimental model that mechanistically links this *SCN5A* dysfunction to atrial conduction defects, reentry formation, and antiarrhythmic drug response has been lacking. While slowing of atrial conduction is a known consequence of sodium channel deficiency (*6*), it remains unclear whether reduced excitability alone is sufficient to sustain complex reentrant circuits (the functional hallmark of AF) in the human atrium, or if additional structural remodeling is required to establish a reentry-permissive substrate.

Unraveling these mechanisms requires a human experimental model capable of recapitulating both the genetic complexity and the macroscopic propagation dynamics of the fibrillating atrium. In our previous study using induced pluripotent stem cell-derived ventricular cardiomyocytes (iPSC-CM) carrying the same heterozygous *SCN5A* p.S1812X truncation, we demonstrated a marked reduction of I_{Na} and disrupted connexin 43 (Cx43) membrane localization, confirming the strong functional and structural impact of this variant (*7*). However, direct human evidence linking this chronic $Na_V1.5$ deficiency to specific atrial conduction defects and reentry formation has not been established. Current research platforms have been hindered by technical limitations. Animal models often fail to replicate human atrial electrophysiology, while human iPSC-atrial-CMs (iPSC-aCMs) have largely been restricted to single-cell phenotyping, small-scale clusters, or models reliant on optical mapping (*8-12*). Recent advances using conditionally immortalized atrial myocytes have generated 2D sheets capable of supporting reentry (*13*). However, characterizing these arrhythmias typically relies on optical voltage mapping. This approach, while powerful, is inherently limited by phototoxicity and dye instability, preventing the observation of sustained arrhythmia dynamics over clinically relevant timescales (*14*). Furthermore, conventional microelectrode arrays (MEAs) are constrained by a limited active recording area, often failing to encompass the full trajectory of reentrant circuits or track meandering rotors across the macroscopic syncytium.

To bridge this gap, we developed a label-free, high-density microelectrode array (HD-MEA) platform capable of continuous, long-term mapping of excitation propagation across large-

scale human atrial monolayers (*15*). By integrating 512 microelectrodes with a spatial resolution sufficient to resolve wavefront curvature and local block (*15*), this system overcomes the blind spots of conventional MEAs and the temporal limits of optical mapping. This technology allows us to capture the initiation, maintenance, and termination of stable reentrant circuits in a strictly controlled human in vitro environment.

In this study, we combined this HD-MEA platform with patient-specific iPSC-aCMs derived from the same *SCN5A* p.S1812X carriers and, crucially, a genotype-negative BrS patient (BrS3) as a clinical comparator to distinguish mutation-specific effects from general disease background. We demonstrate that *SCN5A* haploinsufficiency creates an arrhythmogenic substrate driven by the concomitant loss of I_{Na} density and heterogeneous Cx40 gap-junctional remodeling. This specific combination renders the atrial syncytium highly susceptible to both spontaneous and pacing-induced sustained micro-reentry (> 30 s) spinning at clinically relevant frequencies (~6 Hz), a severe phenotype notably absent in genotype-negative and healthy control lines. Furthermore, by subjecting these reentry-in-a-chip models to clinically used antiarrhythmic agents, we validate the platform as a mechanism-based assay for distinguishing rhythm-control from rate-control strategies, paving the way for precision pharmacology in Brugada-associated AF.

RESULTS

Clinical relevance. Previously, we established patient-specific iPSC lines from one male BrS patient (BrS1) and his biological sister (BrS2), and their ventricular phenotypes were characterized in our earlier study (*7*). Both patients were treated with an implantable cardioverter-defibrillator. Genetic screening for possible mutations in several cardiac-specific genes revealed the heterozygous *SCN5A* point mutation C > A at position c.5435 in both patients (*16*).

In this study, we also included another BrS patient BrS3 (initially named iBrS2 in our previous publication Veerman et al. 2016) without any novel or rare variants in genetic screening of the coding region of *SCN5A* (*17*). Furthermore, the BrS3 patient was negative for such variants in all other BrS-associated genes. However, the BrS3 patient was an elderly male with a history of syncope who presented with episodes of paroxysmal atrial fibrillation (*17*). In the patient's family, sudden cardiac death was reported in several members (*17*).

Three cell lines derived from 3 independent healthy individuals were used as Ctrl cell lines (*18*). None of the individuals were ever diagnosed with cardiovascular disease. All the detailed information about the patients and healthy donors is listed in Table S1.

$Na_V1.5$/Cx40 remodeling in BrS1/2-aCMs

Using our previously established atrial differentiation method (*19*), we successfully differentiated iPSCs into atrial CMs with high purity. Briefly, iPSCs were first treated with CHIR and IWP2 to modulate canonical WNT signaling, followed by treatment with 1 μM retinoic acid at days 3-6 for atrial subtype specification (Fig. 1A). Flow cytometry detected 94.6% Ctrl-CMs, 94.2% BrS1-aCMs, 96.5% BrS2-aCMs, and 96.8% BrS3-aCMs positive for cTnT (Fig. 1B and C). Immunofluorescence staining for MLC2V and MLC2A revealed that RA-treated cultures (iPSC-aCMs) showed prominent expression of MLC2A (Fig. 1D).

Consistent with our previous study in ventricular cardiomyocytes (*7*), we applied an antibody that detects truncated proteins of $Na_V1.5$ to study whether the p.S1812X mutation affected the cellular localization of $Na_V1.5$ in BrS-aCMs (Fig. 1E). Control cells exhibited the expected continuous membrane-associated $Na_V1.5$ pattern, with only minimal cytosolic signal. In contrast, both BrS1 and BrS2 cultures showed a markedly disrupted pattern characterized by intermittent membrane labeling, coarse clustering, and increased intracellular signal, consistent with impaired trafficking and surface expression of truncated $Na_V1.5$ (*20, 21*). BrS3-aCMs, in line with their genotype-negative status, displayed a preserved membrane-localized Nav1.5 distribution similar to controls and lacked the fragmented pattern observed in BrS1/2.

In contrast to our previous study in ventricular cardiomyocytes, we examined connexin 40 (Cx40) rather than Cx43, consistent with the established finding that Cx40 represents the predominant connexin isoform in atrial cardiomyocytes (*22*). While Ctrl-aCMs showed robust and continuous Cx40 labeling along intercellular borders, BrS1 and BrS2 cultures frequently displayed fragmented, punctate, and misaligned Cx40 signal (Fig. 1F). Together, these findings indicate that both sodium-channel and gap-junction architecture are altered in *SCN5A*-mutant BrS-aCMs.

Western blotting confirmed reduced $Na_V1.5$ protein abundance in mutation-positive BrS-aCMs (Fig. 1G and H). When normalized to NaK ATPase, $Na_V1.5$ levels were significantly decreased in BrS2 ($p = 0.0094$, t-test) and showed a strong downward trend in BrS1 ($p = 0.0708$) compared with Ctrl, whereas the genotype-negative BrS3 line exhibited $Na_V1.5$ abundance comparable to that of Ctrl. Total Cx40 protein levels exhibited substantial inter-line variability without a consistent group-wise difference, although immunostaining revealed a more fragmented and discontinuous junctional pattern in BrS1/2-aCMs relative to Ctrl (Fig. 1I).

BrS1/2-aCMs recapitulate sodium channel loss-of-function

Previously, we revealed 50% more I_{Na} reduction in 3-month-cultured BrS ventricular CMs derived from iPS cells carrying the heterozygous *SCN5A* mutation p.S1812X, compared to Ctrl ventricular CMs (*7*). To test whether the *SCN5A* p.S1812X mutation has an effect on iPSC-aCMs, we performed the automated patch-clamp recording under 50 mM $[Na^+]_O$ and found similar results (*7*). Compared to Ctrl-aCMs (-190.1 ± 15.1 pA/pF), the peak I_{Na} density was significantly reduced in BrS1-aCMs (-101.6 ± 8.5 pA/pF, $p < 0.0001$) and BrS2-aCMs (-77.5 ± 8.0 pA/pF, $p < 0.0001$) under -30 mV stimulation (Fig. 2 A-C). In contrast, BrS3-aCMs had a Ctrl-comparable I_{Na} density at -30 mV (-213.7 ± 16.4 pA/pF). As observed for steady-state activation in ventricular BrS-CMs (*7*), BrS1/2-aCMs also showed a rightward shift in the curves, whereas BrS3-aCMs did not (Fig. 2D). However, the $SCN5A^{p.S1812X}$ mutation did not affect the steady-state inactivation curves of atrial CMs (Fig. 2D), similar to observed in our ventricular CMs study (*7*). To determine whether the I_{Na} recorded in aCMs remains sensitive to the sodium channel blocker tetrodotoxin (TTX), we applied 2.5 μM TTX to Ctrl-aCMs to block I_{Na}. I_{Na} density at -25 mV was significantly reduced by 41% from -152.6 ± 20.4 pA/pF to -89.7 ± 13.2 (Fig. 2E and F).

The deficient I_{Na} in BrS1/2-aCMs prompted us to examine the action potential (AP) since I_{Na} is responsible for the upstroke velocity (Vmax) in AP depolarization phase 0 (Fig. 2G-I). Compared with the minute-long stable APs observed in Ctrl-CMs (97.5%), arrhythmic APs, including delayed afterdepolarizations (DADs) and DAD-triggered activities, were exhibited in 34.3% of BrS1-aCMs and 33.3% of BrS2-aCMs (Fig. 2G and H). In contrast, BrS3-aCMs, which harbor no *SCN5A* mutation, maintained rhythmic beating at a rate of 97.5%. I_{Na} deficiency indeed resulted in a significant decrease in the Vmax of BrS1-aCMs (7.5 ± 0.5 V/s, $p = 0.02$) and BrS2-aCMs (7.3 ± 0.4 V/s, $p = 0.02$) compared to Ctrl-aCMs (23.9 ± 4.9 V/s, Fig. 2I). In contrast, BrS3-aCMs had a Ctrl-comparable Vmax (22.8 ± 5.6 V/s, Fig. 2I). Additionally, there were no significant differences in resting membrane potential (RMP) or AP amplitude (APA) between Ctrl-aCMs and any of the BrS lines (BrS1/2/3-aCMs) (Fig. 2I).

Manual recording of APs at 35°C showed similarly spontaneous beating frequencies (average of approximately 2 Hz) among Ctrl-aCMs, BrS1-aCMs, BrS2-aCMs, and BrS3-aCMs (Fig. 2I). Under 2 Hz pacing, the APD_{90} among Ctrl-aCMs (194.1 ± 8.4 ms), BrS1-aCMs (200.7 ± 10.1 ms), BrS2-aCMs (198.5 ± 7.7 ms), and BrS3-aCMs (196.6 ± 11.3 ms) were comparable (Fig. 2I). The spontaneous beating rate (~2 Hz) and APD_{90} (~200 ms) confirmed a robust atrial electrophysiological phenotype.

Conduction slowing in BrS1/2-aCM cultures

To visualize the conduction propagation, we applied our developed HD-MEA platform and scripted a vector-based CV analysis module in our field potential recording software, where the arrow indicates the direction of signal propagation and the length indicates the value of the CV (Fig. 3A-F). Using the same criteria (threshold, vector scale, and arrow size) for vector plotting, we can easily observe a dramatic difference between Ctrl-aCM and BrS1/2-aCM cultures (Fig. 3A and D), where the predominant direction of propagation is anisotropic in Ctrl-aCMs but is isotropic in BrS1/2-aCMs. To dynamically view the beat-to-beat CV changes, we improved our software to plot all beats using box and whisker plots (Fig. 3C and F). In order to reasonably quantify the CV of a culture, we calculated the median value of each beat to represent the CV of that beat, and averaged all stable medians to represent the CV value of the culture. We found that the CVs of BrS1-aCM (18.1 ± 1.0 cm/s, $p < 0.0001$) and BrS2-aCM (13.3 ± 1.1 cm/s, $p < 0.0001$) cultures were significantly slower than that of Ctrl-aCM cultures (30.0 ± 1.3 cm/s, Fig. 3C, F and J). In contrast, BrS3-aCMs had a Ctrl-comparable CV (28.7 ± 1.8 cm/s). Frame-by-frame dissection of normalized voltage and phase maps revealed a spread of sodium spikes across the electrode distribution area of 95.3 mm^2 (Fig. 3G-I), spending 30-40 ms in Ctrl-aCM (Fig. 3G) and BrS3-aCM cultures (Fig. 3I), compared to a prolonged 70-80 ms in BrS1/2-aCM cultures (Fig. 3H) for one spontaneous beating. Furthermore, spatial map of activation time confirmed the conduction slowing in BrS1/2-aCM cultures compared to Ctrl-aCMs (Fig. 3B and E). We observed an overlay of sodium spikes for all detectable channels in Ctrl-aCM culture over a time frame of about 30 ms, with time as the x-axis, but sodium spikes are distributed over a longer time frame of about 70 ms in BrS1/2-aCM, which is again confirmed by the inserted spatial activation maps (fig. S1B and E). For field potential amplitude and slope quantification, we averaged all detectable sodium spikes for one beat, and averaged all mean values of all beats to represent one culture (fig. S1C and F). The data scatter of field potential amplitude and slope showed a similar pattern to CV, confirming the sodium current deficiency in BrS1/2-aCMs, but not in BrS3-aCMs (Fig. 3K and L). The beating frequencies were comparable among the four groups (Fig. 3M), consistent with the frequencies observed in manual patch-clamp recordings.

BrS1/2-aCM cultures were vulnerable to pacing-induced reentrant arrhythmias

To avoid the limitations of external commercial or homemade pacers such as imprecise positioning, variable distance, batch-to-batch inconsistency, and potential damage to the cultures (*14*), we integrated stimulation electrode paddles directly onto the four edges of the HD-MEA chip (Fig. 4A) (*15*). We positioned a larger grounding paddle near each stimulation electrode to conductively dissipate pacing-induced currents and eliminate stimulation artifacts

(Fig. 4A). We then designed a protocol with stepwise increasing pacing rates (4-6-8-10 Hz) to induce reentrant arrhythmias (Fig. 4B). Since the HD-MEA chip contains four stimulation paddles positioned at its corners, we designed a pacing regime to quantify the reentrant arrhythmias susceptibility in Ctrl- and BrS-aCMs (Fig. 4C). Prior to study pacing, all cultures were loaded into the HD-MEA system to record spontaneous beats for 1 min to assess spontaneous reentrant arrhythmias. To systematically provoke reentrant events, stimulation paddles were activated sequentially using a manual protocol to ensure precise control over the induction process. While this approach introduced variable intervals between pacing steps, it offered a decisive experimental advantage: the ability to instantly halt stimulation once a reentrant event was triggered. This strategy prevented the masking or termination of induced arrhythmias often caused by rigid automated protocols, thereby maximizing the capture rate of sustained reentry.

All (100%) Ctrl-aCM cultures exhibited spontaneous pacemaker rhythm and 95.5% (21 out of 22) were resistant to pacing-induced reentrant arrhythmias (Fig. 4D-E and G). Although we observed in 1 out of 22 Ctrl-CM cultures pacing-induced reentrant arrhythmia (Fig. 4E) after stimulation of paddle 2 (a reentry with less than 5 s) and 3 (a reentry with less than 1 s), we did not observe any sustained reentries in Ctrl-aCM cultures.

In contrast, spontaneous reentrant arrhythmias were observed in 40.7% (11 out of 27) BrS1-aCM and 26.5% (9 out of 34) BrS2-aCM cultures, but not in BrS3-aCMs (Fig. 4G). Additionally, a large number of pacing-induced reentrant arrhythmias occurred in 18.5% (5 of 27) of BrS1-aCM cultures and 29.4% (10 of 34) of BrS2-aCM cultures (Fig. 4F-G) whereas pacing-induced reentrant arrhythmias exhibited in 10% (3 out of 30) BrS3-aCM cultures. Magnitude and phase maps clearly visualize the transition from linear pacemaker rhythm to a rotor-patterned reentrant arrhythmia by pacing in BrS-aCM cultures (Fig. 4F). Dynamic visualization of a representative sustained reentrant episode from a BrS-aCM culture is provided in Movies S1 (raw traces) and S2 (magnitude and phase maps), which depict the same reentrant episode.

To systematically compare reentry susceptibility across cultures, we quantified the proportion of cultures exhibiting (i) any reentry, (ii) non-sustained reentry (< 5 s), and (iii) sustained reentry (> 30 s) (Fig. 4H). Clinically relevant sustained reentry (> 30 s), which reflects a robust and self-maintaining arrhythmogenic substrate, occurred predominantly in the BrS1/2 groups. All of cultures with reentrant arrhythmias in BrS1/2-aCM cultures showed as sustained reentry (> 30 s), highlighting their markedly increased reentry stability (Fig. 4H). In BrS3-aCM cultures, one case revealed non-sustained reentry and two cases with sustained reentry (Fig.

4H). The reentrant appearance rate in BrS3-aCM cultures is much lower than BrS1/2, but higher than Ctrl. However, the underlying mechanism for the AF susceptibility in non-*SCN5A* mutant BrS3-aCM cultures remains elusive.

Moreover, Ctrl-aCM cultures exhibited highly synchronized pacemaker-like activity across the 512-electrode array (fig. S2A-B). The field potential traces showed regular, rhythmic depolarizations with nearly uniform amplitude and timing, indicating homogeneous electrical coupling among neighbouring cells (fig. S2B). The 3D waterfall visualization further confirmed the synchronous propagation of field potentials, reflecting stable automaticity and coordinated activation in the control atrial syncytium (fig. S2C). In contrast, the reentry in BrS-aCM cultures displayed markedly irregular and desynchronized field potential patterns with high frequency rotation (4-5 rotations per second, fig. S3). The overlay and 3D waterfall plots revealed asynchronous activation across the array, suggesting localized conduction block and fragmented wavefront propagation (fig. S3B and C). These electrophysiological features closely resemble reentrant arrhythmia dynamics in BrS.

Furthermore, to quantitatively assess the dynamics of reentrant activity, the reentry frequency was analyzed across all cultures. When data from all reentry-positive cultures were pooled regardless of genotype (BrS1/2/3), the mean reentry frequency was approximately 5.8 ± 0.2 Hz (fig. S4A, n = 38). Nevertheless, as shown in the scatter plot in fig. S5B, no significant difference in reentry frequency was observed between spontaneous and pacing-induced reentries within BrS1/2/3-aCM cultures. Because only one out of 22 Ctrl-aCM cultures exhibited pacing-induced reentry (with a frequency of 9.4 Hz), statistical comparison between Ctrl and BrS was not meaningful.

Acute sodium channel blockade fails to recapitulate the reentrant phenotype in Ctrl- and genotype-negative BrS3-aCM cultures

To test our hypothesis that sodium current reduction alone is insufficient to cause the high reentry vulnerability observed in BrS1- and BrS2-aCM cultures, we applied 2.5 μM TTX to Ctrl- and BrS3-aCM cultures (Fig. 5A). In Ctrl-aCM cultures, TTX significantly slowed the CV from 30.4 ± 1.3 cm/s to 18.5 ± 1.1 cm/s (Fig. 5B-D). Concurrently, field potential amplitude, slope, and beating frequency were significantly reduced (Fig. 5D). We then examined whether this acute conduction slowing could promote arrhythmia. Under basal conditions, all 20 Ctrl-aCM cultures exhibited stable pacemaker-like field potentials, and only one culture developed pacing-induced reentry (Fig. 5F). However, TTX exposure for 30 min, despite the marked reduction in excitability, did not induce any reentrant appearance in Ctrl cultures (Fig. 5E and F).

We further extended this validation to the genotype-negative BrS3. Although the donor presented with clinical AF, BrS3-aCMs exhibit normal I_{Na} density and lack the structural defects seen in *SCN5A*-mutant lines. Consistent with the results in Ctrl, no spontaneous or pacing-induced reentry was detected in a cohort of 18 BrS3-aCM cultures under basal conditions (Fig. 5G). Crucially, even after restricting I_{Na} availability with 2.5 μM TTX, all 18 BrS3-aCM cultures remained resistant to reentry induction (Fig. 5G). These results strongly suggest that reduced excitability alone is insufficient to establish a sustained reentrant substrate in the absence of chronic structural remodeling.

HD-MEA as a platform to test anti-AF drugs using BrS1/2-aCM cultures

Given that all spontaneous and pacing-induced reentrant arrhythmias in BrS1/2-aCM cultures were sustained (> 30 s) (Fig. 4G and H), we applied different antiarrhythmic drugs to sustained reentrant cultures in the following studies. Vernakalant is an antiarrhythmic drug licensed for pharmacological cardioversion of recent-onset AF. Continuous field-potential recordings showed that reentry remained stable before drug administration, but its rotation frequency gradually reduced during exposure to 3 μM vernakalant and further during 10 μM treatment, ultimately leading to rhythm destabilization (Fig. 6A). After approximately 800 seconds of vernakalant exposure, the reentrant spiral wave abruptly transitioned into a pacemaker spontaneous rhythm (Fig. 6B). This drug-induced rhythm conversion closely parallels the clinical strategy of rhythm control, in which atrial fibrillation is terminated and normal organized beating is restored. Vernakalant converted reentry to pacemaker-like activity in a concentration-dependent manner with 33.3% at 10 μM (3 out of 9) and 44.4% (4 out of 9) at 30 μM in BrS1/2-aCM cultures (Fig. 6C). Baseline rotation frequency (6.8 ± 0.5 Hz) was calculated from all cultures exhibiting reentry before treatment. After exposure to 30 μM vernakalant, rotation frequency was reduced to 4.4 ± 0.2 Hz in the cultures that continued to sustain reentry, whereas cultures that converted to pacemaker rhythm were excluded from the post-treatment analysis (Fig. 6D). These data indicate that acute perfusion of vernakalant led to a progressive slowing of spiral-wave rotation in BrS1- and BrS2-aCM cultures.

Flecainide is an antiarrhythmic medication to treat paroxysmal supraventricular tachycardia, a potentially life-threatening irregular arrhythmia. In our study, flecainide converted reentry to pacemaker-like activity in 35.7% of BrS1/2-aCM cultures (5 out of 14 cultures). Baseline rotation frequency (5.6 ± 0.3 Hz) was calculated from all cultures exhibiting reentry before treatment. After exposure to 20 μM flecainide, the rotation frequency was reduced to 2.2 ± 0.1 Hz in the cultures that continued to sustain reentry, whereas cultures that converted to

pacemaker rhythm were excluded from the post-treatment analysis (Fig. 6E-G). These data are comparable to those derived from vernakalant treatment.

Propranolol is a medication of the beta-blocker class. It is used to treat high blood pressure and various types of arrhythmias. Different from vernakalant/flecainide, the rate-controlling class II antiarrhythmic agent propranolol reduced rotation frequency from 5.9 ± 0.3 Hz to 3.1 ± 0.2 Hz after 10 μM propranolol treatment in BrS-aCM cultures, but failed to terminate reentry (Fig. 6H-K).

Although spontaneous reentry was absent in BrS3-aCMs, high-frequency pacing successfully induced sustained reentry (>30 s) in a small subset of cultures (2 out of 30). We utilized these two cases to test the efficacy of the atrial-selective antiarrhythmic vernakalant. In one culture, perfusion of 30 μM vernakalant successfully destabilized the reentrant circuit and restored sinus rhythm (fig. S5A). However, the second culture remained refractory, with sustained reentry persisting (fig. S5B). These data suggest that once a reentrant substrate is established, its pharmacological sensitivity is comparable across genotypes.

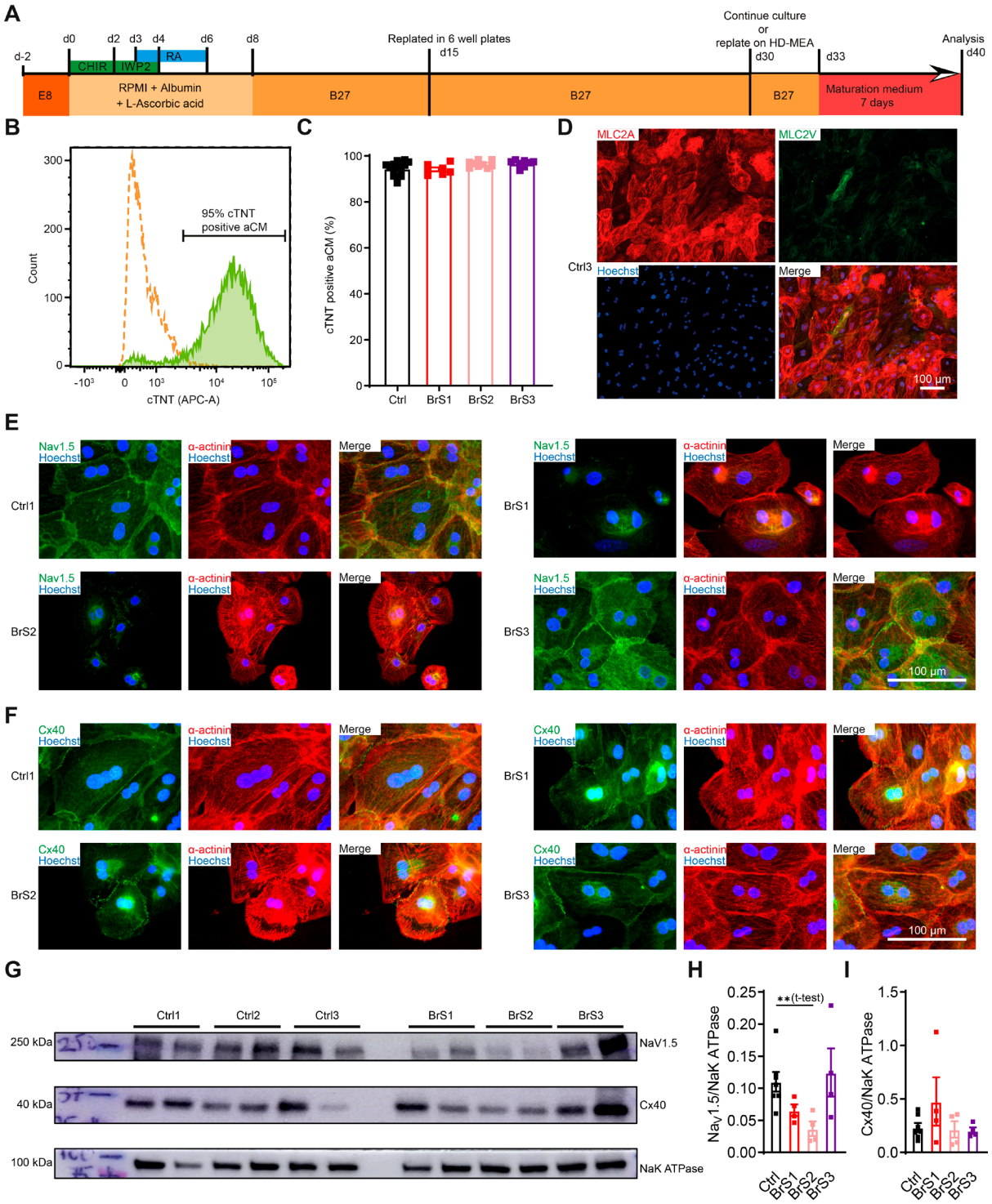

Fig. 1. Atrial cardiomyocyte differentiation and $Na_V1.5$/Cx40 remodeling. (**A**) Scheme of the directed differentiation protocols. Retinoic acid (RA) was used to induce the atrial subtype differentiation. (**B**) Representative flow cytometry traces for one atrial differentiation. (**C**) Proportion of cTnT-positive aCMs (Ctrl: 15 independent differentiations of 3 cell lines; BrS1: 7 independent differentiations of 2 cell lines; BrS2: 9 independent differentiations of 2 cell lines; BrS3: 8 independent differentiations of 2 cell lines). (**D**) Double-immunostaining of myosin light chain 2, ventricular/atrial isoforms in atrial-iPSC-CMs. Cell nuclei are shown in blue (Hoechst 33342). Scale bar: 100 µm. (**E**)

Double-immunostaining of Ctrl1- and BrS1, 2, and 3-aCMs with antibodies against $Na_V1.5$ and α-actinin. Scale bar, 100 μm. (**F**) Double-immunostaining of Ctrl1- and BrS1, 2, and 3-aCMs with antibodies against Cx43 and α-actinin. Scale bar, 100 μm. (**G**) Representative Western blots showing $Na_V1.5$, Cx40, and NaK ATPase expression in Ctrl and BrS iPSC-aCM cultures. (**H**) Quantification of $Na_V1.5$ band intensity normalized to NaK ATPase ($Na_V1.5$/NaK ATPase). (**I**) Quantification of Cx40 band intensity normalized to NaK ATPase (Cx40/NaK ATPase). Predefined comparisons (Ctrl vs BrS1 and Ctrl vs BrS2) were analyzed using a two-tailed unpaired t-test. Data are presented as mean ± SEM; each point represents one cell-line batch. $^{**}p < 0.01$.

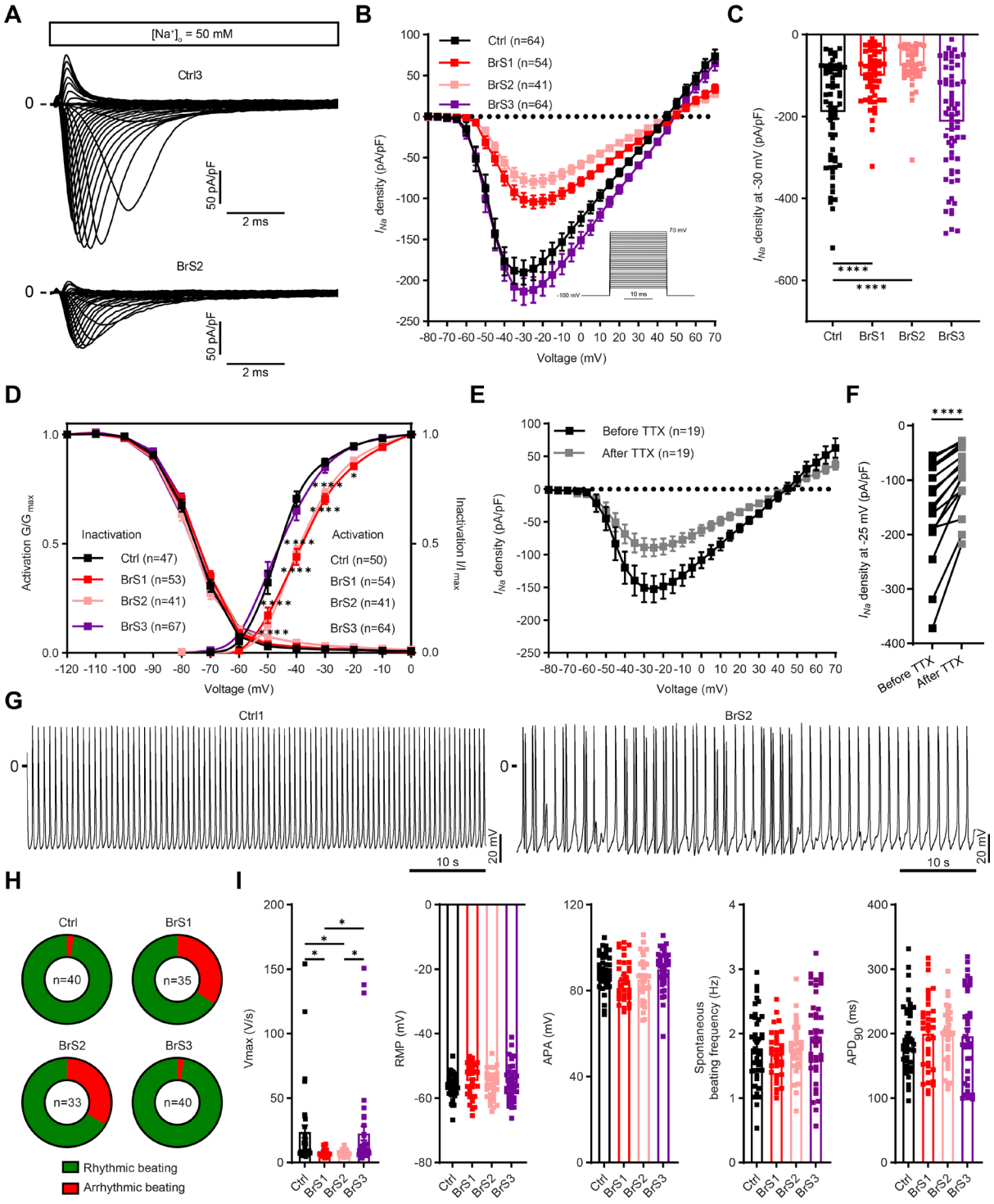

Fig. 2. Electrophysiological characterization of Ctrl-aCMs and BrS-CMs. (**A**) Automated patch-clamp recordings of I_{Na} under low extracellular sodium concentration (50 mM $[Na^+]_O$) in representative Ctrl3 and BrS2 cells. (**B**) The I-V curve of I_{Na} (Ctrl: 64 cells from 7 independent differentiations of 3 cell lines; BrS1: 54 cells from 6 independent differentiations of 2 cell lines; BrS2: 41 cells from 6 independent differentiations of 2 cell lines; BrS3: 64 cells from 6 independent differentiations of 2 cell lines). The stimulation protocol is shown as an inset. (**C**) The scatter plot shows I_{Na} density at -30 mV. (**D**) The activation and inactivation curves of I_{Na}. I-V curves (**E**) and scatter plot (**F**) of I_{Na} in Ctrl-aCMs

365 before and after 2.5 μM TTX treatment (data come from 5 independent differentiations of 3 Ctrl cell
366 lines). (**G**) Shown are representative traces of spontaneous APs for Ctrl1- and BrS2-aCM. (**H**)
367 Percentage of Ctrl- and BrS-aCMs exhibiting spontaneous rhythmic or arrhythmic beating. (**I**)
368 Quantification of key AP metrics: *V*max, RMP, and APA, spontaneous beating frequency and APD_{90}
369 at 2 Hz pacing (Ctrl: 40 cells from 8 independent differentiations of 3 cell lines; BrS1: 35 cells from 6
370 independent differentiations of 2 cell lines; BrS2: 33 cells from 6 independent differentiations of 2 cell
371 lines; BrS3: 40 cells from 6 independent differentiations of 2 cell lines). Data are presented as mean ±
372 SEM. Two-way ANOVA with Sidak's post-test was used for I_{Na} analysis. Two-tailed paired Student's
373 t-test was used for TTX treatment analysis. One-way ANOVA with Tukey's post-test was used for AP
374 analysis. *$p < 0.05$; **$p < 0.01$; ***$p < 0.001$; ****$p < 0.0001$.

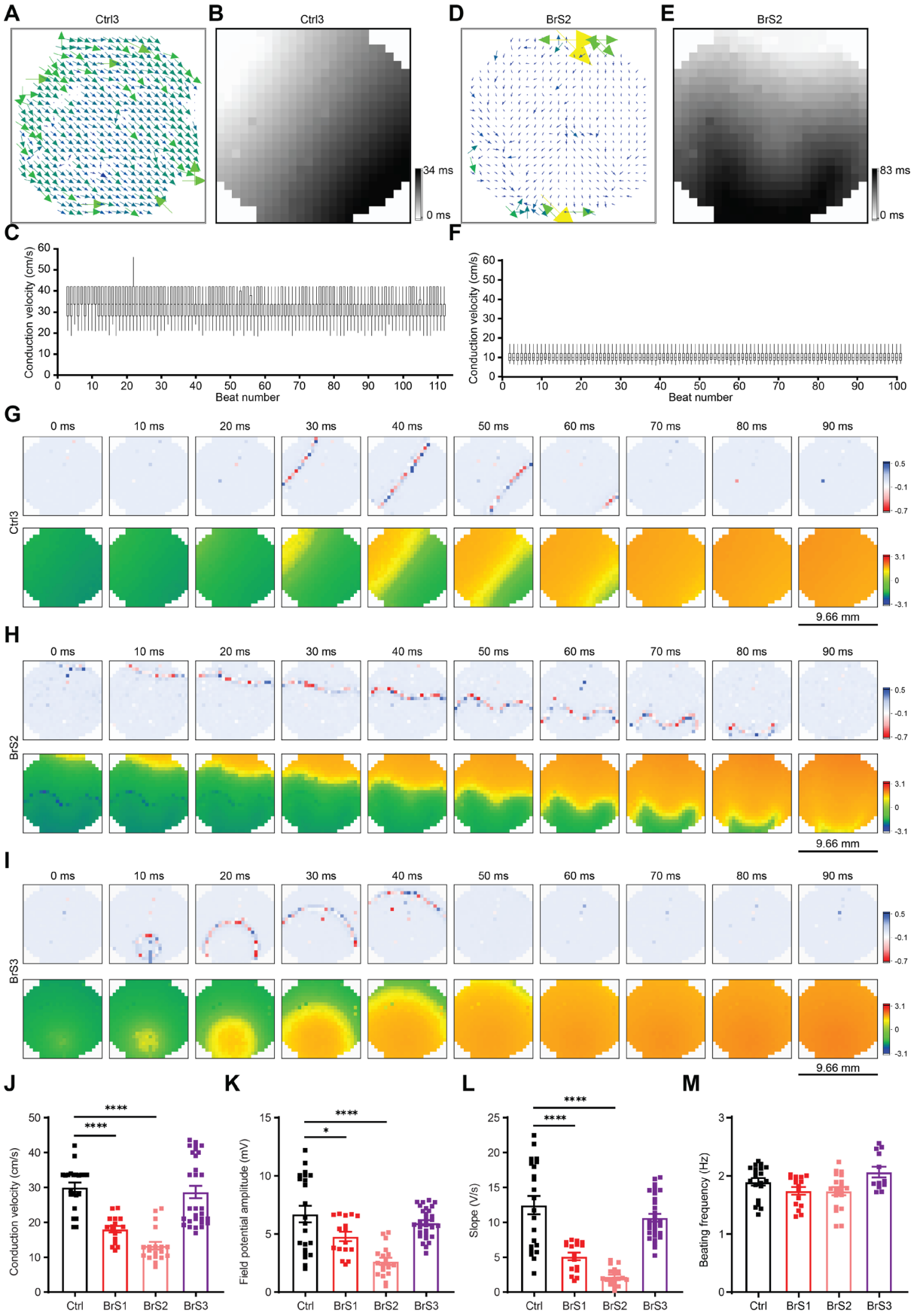

Fig. 3. Spontaneous field potential characterization on HD-MEA. (**A**) Shown is CV vector map for one spontaneous beating Ctrl3-aCM culture on HD-MEA. The arrow indicates CV direction and length

indicates conduction speed. (**B**) Spatial map of activation time for one spontaneous beating Ctrl3-aCM culture on HD-MEA. (**C**) Box and whisker plot for CV beat-to-beat during one-minute recording of spontaneous beating in one Ctrl3-aCM culture. The median value of one beat was chosen to represent the CV of the beat. (**D**) Shown is CV vector map for one spontaneous beating BrS2-aCM culture on HD-MEA. (**E**) Spatial map of activation time for one spontaneous beating BrS2-aCM culture on HD-MEA. (**F**) Box and whisker plot for CV beat-to-beat during one-minute recording of spontaneous beating BrS2-aCM culture. Normalized voltage and phase maps of representative beats in Ctrl3-aCM (**G**), BrS2-aCM (**H**) and BrS3-aCM (**I**) cultures were profiled frame by frame (in 10 ms increments). The metrics of HD-MEA measurements including CV (**J**), field potential amplitude (**K**), field potential slope (**L**), and beating frequency (**M**) in Ctrl-aCMs, BrS1/2/3-aCM cultures (Ctrl: 22 cultures from 11 differentiations of 3 cell lines; BrS1: 16 cultures from 4 differentiations of 2 cell lines; BrS2: 19 cultures from 7 differentiations of 2 cell lines; BrS3: 30 cultures from 8 differentiations of 2 cell lines). Data are mean ± SEM. One-way ANOVA followed by Dunnett test was used for statistical analysis.

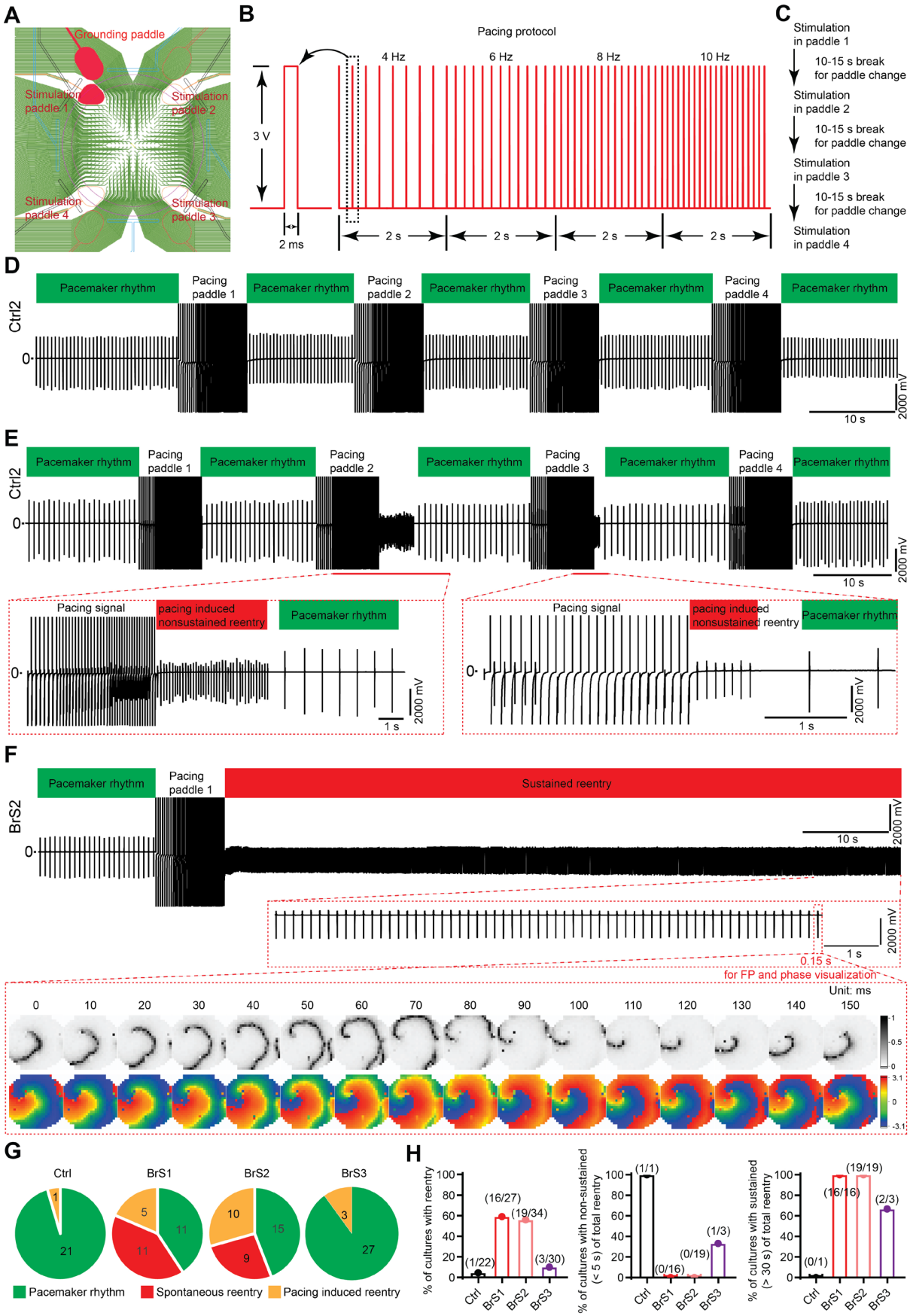

Fig. 4. Atrial reentrant arrhythmia characterization. (**A**) The layout of the HD-MEA chip shows the integrated stimulation paddles 1, 2, 3 and 4. Four corresponding paddles are distributed nearby to

receive the stimulation artifact charges. (**B**) Illustration of the stepwise pacing protocol (4, 6, 8, 10 Hz) used for reentry induction. (**C**) Scheme of the pacing regime, including paddle selection and brief breaks. (**D**) After pacing session applied in paddle 1, 2, 3 and 4, no reentry was induced in one Ctrl2-aCM culture. (**E**) Non-sustained reentries were induced by pacing in only one Ctrl2-aCMs culture. Enlargement of the highlighted non-sustained reentries (a 4 s reentry and one reentry < 1 s) from panel **E**. (**F**) In one culture of BrS2-aCMs, a sustained reentrant arrhythmia was induced by a pacing session at paddle 1. At the end of the trace BrS2-aCM, 10-s fragment was zoomed out to show the high-frequency reentrant beating. Normalized magnitude and phase maps of representative 150 ms of the last beat recorded in cultures of BrS2-CM were analyzed frame-by-frame (in 10-ms increments) to indicate conversion of a linear pacemaker rhythm to a rotor-pattern reentrant arrhythmia by pacing. (**G**) Percentage of Ctrl- and BrS-aCMs with pacemaker rhythm, spontaneous reentrant arrhythmia and pacing induced reentrant arrhythmia (Ctrl: 22 cultures in total from 11 independent differentiations of 3 cell lines; BrS1: 27 cultures in total from 5 independent differentiations of 2 cell lines; BrS2: 34 cultures in total from 13 independent differentiations of 2 cell lines; BrS3: 30 cultures in total from 8 independent differentiations of 2 cell lines). (**H**) Quantification of the proportion of cultures showing non-sustained reentry (< 5 s) and sustained reentry (> 30 s). Numbers above bars indicate the count of positive cultures relative to the total number of cultures (n/N) and the corresponding percentage.

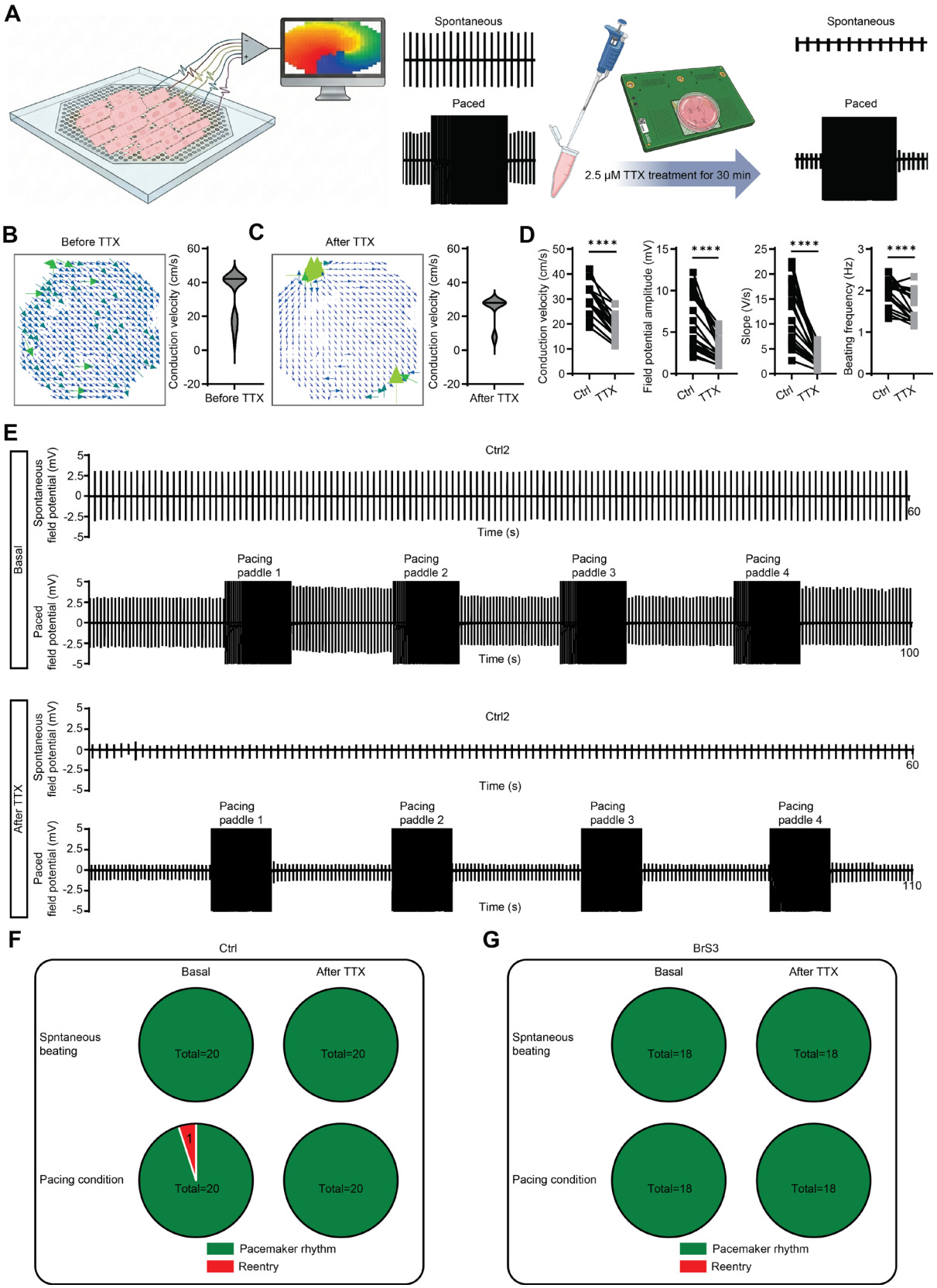

Fig. 5. Assessment of the reentry vulnerability in Ctrl- and BrS3-aCMs cultures upon TTX application. (**A**) The workflow for TTX application in Ctrl- and BrS3-aCM cultures. Created in BioRender. Li, W. (2026) https://BioRender.com/87v80fp. CV vector maps in the Ctrl3-aCM culture before (**B**) and after (**C**) 2.5 μM TTX treatment for 30 min. Violin plots are used to represent the CV of

the corresponding beats before and after TTX treatment. (**D**) Quantifications of CV, field potential amplitude, field potential slope, and beating frequency in Ctrl-aCM cultures before and after TTX treatment (20 cultures from 9 differentiations of 3 cell lines). (**E**) Representative traces of spontaneous beating and pacing-induced activity in one Ctrl2-aCM culture before and after TTX treatment. (**F**) Counting of the spontaneous/pacing-induced reentry in basal and after TTX-treated conditions (20 cultures from 9 differentiations of 3 cell lines). (**G**) Quantification of reentry vulnerability in BrS3-aCM cultures. In a total of 18 cultures (from 4 differentiations of 2 cell lines), no spontaneous or pacing-induced reentry was observed under either basal conditions or following 2.5 μM TTX treatment. Two-tailed paired Student's t-test was used for TTX treatment analysis. ****$p < 0.0001$.

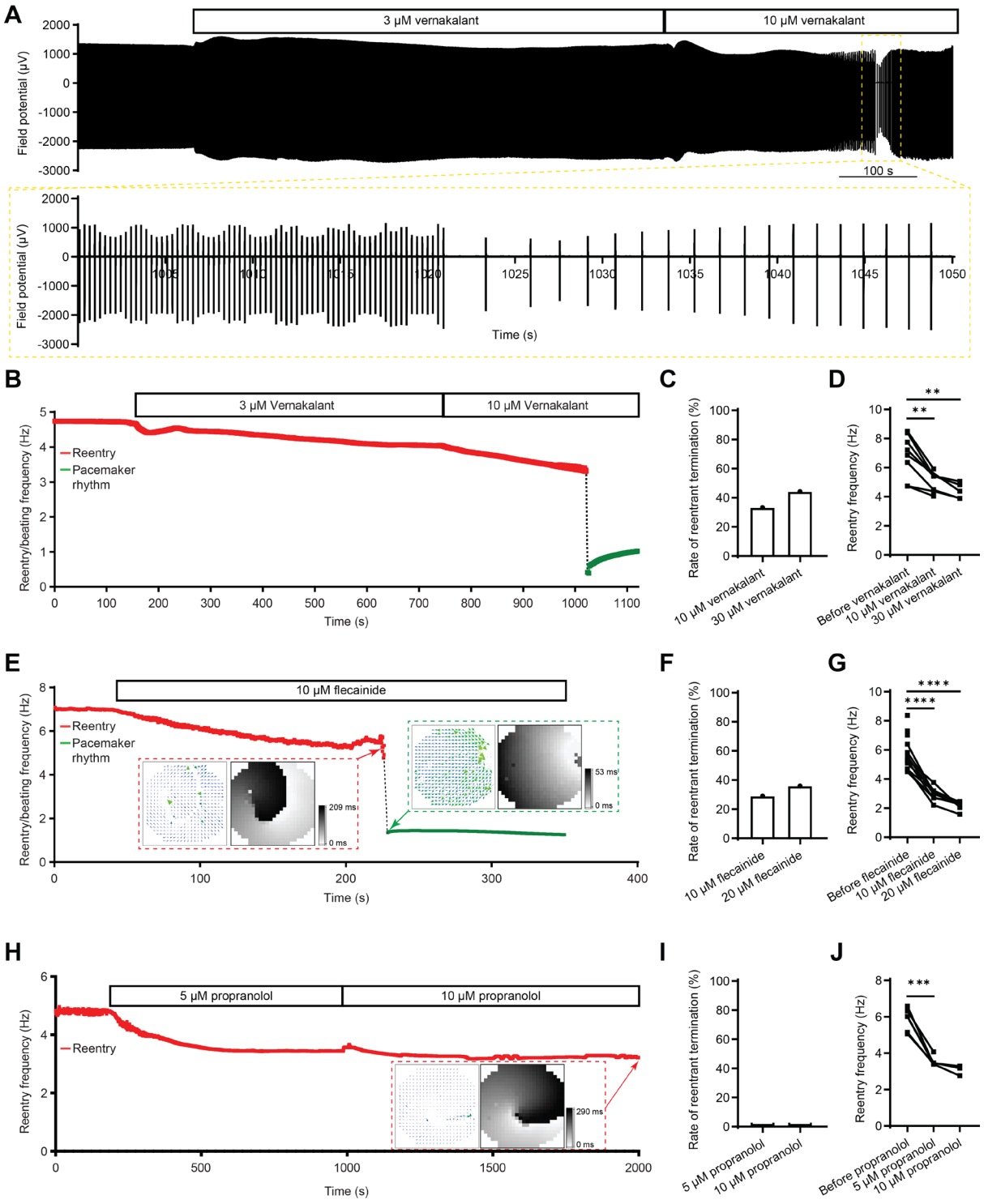

Fig. 6. Testing of antiarrhythmic drugs in BrS-aCM reentry models. (**A**) Randomly selected channel shows the original recording of reentry under vernakalant application. The yellow enlarged region of interest shows the conversion period from reentrant arrhythmia to pacemaker rhythm. (**B**) The instantaneous reentry/beating frequency trace corresponding to panel **A**. Vernakalant (30 μM) converted 44.4% reentrant arrhythmia to pacemaker rhythm (**C**), and reduced rotation frequency in BrS-aCM cultures (**D**) (n = 9 from both BrS1- and BrS2-CM cultures). (**E**) Reentry/beating frequency trace shown the reentry converted to pacemaker rhythm by application of the rhythm-controlling class I

antiarrhythmic agent flecainide. In the red dashed rectangle, the CV vector map and activation map indicate the reentry pattern; in the green dashed rectangle, the CV vector map and activation map indicate the pacemaker pattern. Flecainide converted ~40% the reentrant arrhythmia to pacemaker rhythm (**F**), and reduced rotation frequency in BrS-aCM cultures (**G**) (n = 14 from both BrS1- and BrS2-CM cultures). (**H**) Reentry/beating frequency trace under treatment of the rate-controlling class II antiarrhythmic agent propranolol. In the red dashed rectangle, the CV vector map and activation map indicate the reentry pattern around 2000 s for the last beat. Propranolol did not convert the reentrant arrhythmia (**I**) but reduced rotation frequency in BrS-aCMs (**J**) (n = 6 from both BrS1- and BrS2-CM cultures). Data are presented as mean ± SEM. **p < 0.01; ***p < 0.001; ****p < 0.0001 using student's t-test.

DISCUSSION

In this study, we developed a human AF model of BrS using patient-specific iPSC-aCMs combined with label-free high-density electrophysiological mapping. This platform enabled direct visualization of how *SCN5A* loss-of-function reshapes atrial excitability and conduction to support stable reentry. Mutation-positive BrS atrial cardiomyocytes exhibited reduced $Na_V1.5$ abundance, disrupted membrane targeting, and fragmented Cx40 that translated into slowed, heterogeneous propagation and a markedly lowered threshold for sustained reentry formation. In contrast, the genotype-negative BrS line failed to develop a comparable substrate, underscoring the mutation-specific nature of the phenotype. Moreover, class I like rhythm-control agents reliably decelerated or extinguished rotor dynamics, directly linking sodium-channel deficiency to the functional reversibility of the arrhythmogenic substrate. These findings provide mechanistic insight into BrS-associated AF and highlight the utility of HD-MEA based human models for resolving micro-reentrant drivers.

Mutation-positive BrS1/2-aCMs displayed both functional and structural hallmarks of reduced excitability and enhanced arrhythmia vulnerability. Patch-clamp recordings demonstrated a pronounced reduction in action-potential Vmax, consistent with diminished I_{Na} availability and a right-shifted steady-state activation curve in *SCN5A* loss-of-function cells. BrS1/2-aCMs also showed a significantly higher incidence of spontaneous arrhythmic beating compared with Ctrl-aCMs, reflecting an increased burden of ectopic triggers capable of initiating wavebreaks in a vulnerable substrate (*23*). Resting membrane potential and APD were largely preserved, ruling out global electrophysiological immaturity and indicating that the instability arises specifically from $Na_V1.5$-dependent excitability deficits rather than broad changes in AP morphology (*24*).

At the structural level, BrS1/2-aCMs exhibited clear evidence of sodium channel and gap junction remodeling. $Na_V1.5$ abundance was reduced and its membrane localization was disrupted, indicating impaired surface availability of the channel. Although total Cx40 protein levels were not uniformly decreased, Cx40 junctional organization appeared fragmented, suggesting impaired gap-junction continuity. These combined alterations are expected to slow impulse propagation, reduce source-sink balance, and increase spatial heterogeneity—classic determinants of a reentry permissive substrate (*23-27*).

These molecular and cellular changes were directly reflected in multicellular activation patterns on the HD-MEA platform. In pacemaker-beating conditions, the CV vector mapping signatures aligned closely with the structural remodeling observed in BrS1/2-aCMs, including disrupted $Na_V1.5$ membrane localization and fragmented Cx40 labeling. These findings indicate that the molecular defects translate into a slower, more heterogeneous, and wavebreak-prone conduction substrate. Furthermore, BrS1/2-aCM monolayers exhibited a markedly higher appearance of both spontaneous and pacing-induced reentry. Importantly, the reentry observed in BrS1/2 cultures was fully sustained, with stable rotational activity persisting for hundreds of seconds rather than short-lived or stimulus-dependent spirals. Such long-duration reentry visualization is rarely achieved in human iPSC-derived atrial models and strongly indicates the presence of a robust, mutation-driven reentrant substrate (*9-12*).

Control cultures further emphasized this specificity. All Ctrl-aCM monolayers displayed stable, synchronous pacemaker activity, and only one exhibited two brief, pacing-induced, non-sustained reentry episodes, confirming that the stimulation protocol was not excessively aggressive. Whereas control cultures activated homogeneously across the 512-electrode array, BrS1/2-aCM monolayers displayed fragmented, irregular activation fields, consistent with a destabilized atrial conduction network. Together, these findings indicate that the $Na_V1.5$-p.S1812X mutation destabilizes atrial excitation by concurrently lowering excitability and impairing electrical coupling, thereby lowering the threshold for reentry initiation and enabling arrhythmia-like dynamics even under baseline conditions.

A notable aspect of our study is the inclusion of a genotype-negative BrS3 patient, who presented with a clinical Brugada phenotype and AF but lacked pathogenic variants in *SCN5A* or other recognized BrS-associated genes (*17*). In our model, BrS3-aCMs showed preserved $Na_V1.5$ abundance and normal I_{Na} density comparable to controls. However, unlike the healthy controls which were fully resistant to sustained arrhythmia, the BrS3 phenotype was not entirely quiescent; pacing-induced sustained reentry in a small subset of cultures (2 of 30). Crucially, BrS3-aCMs never exhibited the spontaneous reentry that characterized the *SCN5A*-

mutant BrS1/2 lines. This indicates that while the BrS3 background can sustain reentry upon provocation, it lacks the severe conduction defects required for spontaneous initiation observed in SCN5A loss-of-function models. Interestingly, the pharmacological response of these pacing-induced rotors in BrS3-aCMs was variable, with vernakalant terminating the arrhythmia in one case while failing in the other. This partial efficacy aligns with our findings in BrS1/2-aCMs and highlights the complexity of the arrhythmogenic substrate in Brugada syndrome, where reentrant drivers, once formed, may display heterogeneous responses to sodium-channel blockade. The absence of spontaneous vulnerability in BrS3 underscores the well-known complexity of BrS, in which up to two-thirds of clinically diagnosed cases remain genetically unresolved (*28*). The paroxysmal AF in such genotype-negative patients may arise from variants in less common susceptibility genes, polygenic architectures, or extrinsic modulators (such as fibrosis, autonomic tone, or structural aging) that are not fully recapitulated in isolated iPSC-derived atrial syncytia (*29, 30*). Thus, BrS3 serves as a vital clinical comparator, strengthening the causal link between *SCN5A* truncation and the severe, spontaneously reentrant phenotype characterized in BrS1/2-aCM models.

The activation frequency of reentrant excitation is a key determinant of arrhythmia dynamics and translational relevance (*31*). When quantified across all reentry-positive BrS1/2/3-aCM cultures, the mean reentry frequency was approximately 6 Hz, even in the majority of BrS1/2-aCM cultures carrying the $Na_V1.5$ p.S1812X truncation, which causes approximately a 50% reduction of peak sodium current and consequent conduction slowing. This frequency range is substantially higher than the ~3 Hz reentrant activity reported in early human embryonic stem cell-derived atrial tissue (*32*) and closely matches the 6–8 Hz activation frequencies recorded in atrial fibrillation patients (*13, 31*). Our observed rotational activity mirrors high-frequency driver regions identified in human atrial fibrillation mapping studies, suggesting that our platform captures clinically relevant reentry dynamics.

One of the clearest insights from our study is the distinction between chronic, mutation-driven sodium-channel loss and acute pharmacological block. Partial I_{Na} inhibition with TTX in Ctrl-aCMs uniformly slowed conduction, and decreased FPA and slope, but never produced spontaneous or pacing-induced reentry, indicating that reduced sodium current alone is insufficient to generate a reentrant substrate. This conclusion is further reinforced by our findings in the genotype-negative BrS3-aCMs. Despite the clinical history of AF in the donor, these cells lack the specific *SCN5A*-driven structural remodeling. Consequently, even when their conduction was acutely compromised by TTX, they remained resilient to arrhythmia induction. In contrast, BrS1/2-aCMs exhibit chronic, spatially heterogeneous $Na_V1.5$ loss

together with disrupted membrane targeting and Cx40 remodeling, producing nonuniform excitability and impaired coupling. This patchy conduction reserve creates localized slow-conduction zones and favors unidirectional block, enabling rotor formation and maintenance. Thus, arrhythmogenicity in BrS reflects the combined effects of sodium-channel insufficiency and chronic structural-functional remodeling, rather than the absolute magnitude of I_{Na} reduction.

Both vernakalant and flecainide, two representative class I antiarrhythmic agents, effectively suppressed reentrant activity in BrS1/2-aCM cultures, consistent with their established rhythm-control efficacy in atrial fibrillation (*33-35*). Vernakalant's predominant mechanism in the fibrillating atrium is believed to be rate-dependent inhibition of cardiac sodium channels, complemented by additional blockade of atrial-selective K^+ currents (*36*). These combined actions prolong refractoriness while avoiding excessive conduction slowing (*36*). In our human BrS atrial model, both vernakalant and flecainide destabilized spiral-wave reentry and promoted drug-induced rhythm conversion, closely paralleling the clinical principle of rhythm-control therapy (*37*).

In contrast, the application of propranolol yielded a distinct outcome. Although often classified solely as a Class II beta-blocker, propranolol is well known as a sodium channel blocker. In our model, propranolol significantly reduced the rotor frequency (~50% reduction), confirming its functional block of sodium channels and consequent conduction slowing. However, unlike vernakalant, it failed to terminate the reentry. This differential response highlights a critical biophysical principle: depressing conduction velocity (CV) without sufficiently prolonging the effective refractory period (ERP) decreases the excitation wavelength (wavelength = CV × ERP), potentially allowing the reentrant circuit to fit more easily within the tissue substrate rather than extinguishing it. Thus, our platform successfully distinguishes the mechanistic efficacy of true rhythm-control agents from non-terminating blockade. Together, our genetically defined reentry assay may serve as a foundation for precision electrophysiology, enabling patient- or variant-specific testing of antiarrhythmic compounds (*37*).

In conclusion, we define a human, label-free atrial reentry model that connects *SCN5A*-dependent excitability loss to conduction failure and reentry, and we demonstrate reentry-state pharmacology that distinguishes termination from rate control. By integrating human genetics, stem-cell atrial biology, and high-density electrophysiology, this framework opens a path toward precision electrophysiology and mechanism-based anti-AF drug discovery for Brugada syndrome and beyond.

MATERIALS AND METHODS

Directed differentiation of iPSCs into atrial cardiomyocyte

The study was approved by the Ethics Committee of University Medical Center Göttingen (approval number: 21/1/11 and 10/9/15) and Technical University of Dresden (approval number: EK 422092019) and carried out in accordance with the approved guidelines. We used three independent human iPSC lines as Ctrls, which were previously reprogrammed from somatic cells of three healthy individuals. The cell lines iWTD2.1 (UMGi001-A clone 1), iBM76.3 (UMGi005-A clone 3) and iBrS2-Am2/Am3 (referred to as BrS3 in this study) were generated from dermal fibroblasts, mesenchymal stem cells, and fibroblasts respectively, using STEMCCA lentivirus (*19, 38*). Another cell line, isWT7.22 (UMGi020-B clone 22) was generated from dermal fibroblasts using the integration-free CytoTune-iPS 2.0 Sendai Reprogramming Kit (*39*). Bone marrow derived mesenchymal stem cells and peripheral blood mononuclear cells were cultured and reprogrammed into iPSCs using the STEMCCA lentivirus (BrS1-iPSCs) or Sendai kit (BrS2-iPSCs), as described previously (*7*). Two cell lines were used to represent BrS1, as well as BrS2 and BrS3 to minimize the cell line-to-line variabilities (table S1).

All Ctrl- and BrS-iPSCs were maintained on Geltrex (Thermo Fisher Scientific) coated 6-well plates in Essential 8 medium (Thermo Fisher Scientific) for directed differentiations. Generally, when the iPSCs confluence reached 90% on 12-well plates, the differentiations were initiated with cardio differentiation medium composed of RPMI 1640 with Glutamax and HEPES (Thermo Fisher Scientific), 0.5 mg/ml human recombinant albumin, and 0.2 mg/ml L-ascorbic acid 2-phosphate and treated with 4 μM CHIR99021 (Merck Millipore). After 48 h, CHIR99021 was removed and the cells were treated with 5 μM IWP2 (Merck Millipore). At day 4, IWP2 was removed by medium change to cardio differentiation medium. For atrial subtype differentiation, 1 μM retinoic acid (Sigma-Aldrich) was supplemented at days 3-6 during differentiation. First beating atrial CMs appeared at day 8, and the medium was changed to RPMI/B27 medium (RPMI 1640 with Glutamax, HEPES, and 2% B27, Thermo Fisher Scientific). According to the culture regime (Fig. 1**A**), the differentiated atrial CMs were cultured under RPMI/B27 medium and maturation medium for further analysis.

Automated patch clamp analysis

At the end of the culture regime (day 40), iPSC-aCMs were dissociated into single cells in suspension for automated patch-clamp I_{Na} recording as described in our previous publications(*40, 41*). Briefly, iPSC-aCM cultures were treated with 20 U/mL papain (Sigma-Aldrich) dissolved in 1.1 mM EDTA-buffered B27 medium containing 2.5 μM blebbistatin. After gentle pipetting, cell suspensions were centrifuged at 50g for 1 min, then resuspended in 2.5 μM blebbistatin-buffered B27/RPMI medium at 4 ℃ for 1 hour.

Automated patch-clamp I_{Na} recording was performed at room temperature using Patchliner Quattro (Nanion technologies GmbH) with low resistance NPC-16 chips (Nanion technologies GmbH). The pipette and extracellular solutions are listed in table S2. The dissociated iPSC-aCMs were loaded into Patchliner and depolarised from a holding potential of -100 mV using voltage steps from -80 to +70 mV for 20 ms in 5 mV steps. The sweep interval was 2 s. Currents were sampled at 25 kHz and low-pass-filtered at 2.9 kHz. I_{Na} density was calculated as current normalized to membrane capacitance. For the conductance (G/Gmax) calculation, a custom-built-in formula and add-in module in Excel were used. The same fit functions were used for analyzing the kinetics of I_{Na}. Steady-state activation and inactivation curves were fitted with a standard Boltzmann function: $Y = 1/[1 + \exp((V1/2 - V)/k_\infty)]$, where $V1/2$ is the half-maximal voltage of steady-state (in)activation and k_∞ is the slope factor of the voltage dependence of (in)activation.

Manual patch clamp analysis

On day 32, iPSC-aCMs were trypsinized and plated onto Ø5 mm coverslips in cardiac digestion medium (80% RPMI/B27 + 20% FBS) supplemented with 1 μM TZV. On the second day after digestion, the medium was changed from cardiac digestion medium to maturation medium and recovered for 7 days. At day 40, manual patch clamp technique was used for AP recordings with the EPC10 amplifier (HEKA Elektronik) using the Patchmaster software (HEKA Elektronik) as previously described(*42*). The pipette and extracellular solutions used for AP recordings are listed in table S2.

Spontaneous APs (without current injection) and paced APs were recorded under current-clamp mode in Tyrode's solution at 35 ℃. To assess AP duration (APD), a negative current was injected into the CMs to maintain the RMP at approximately -80 mV prior to application of 2 Hz pacing stimulation. Signals were filtered with 2.9 and 10 kHz Bessel filters. At least 5 consecutive stable spontaneous APs and paced APs were averaged to determine RMP, Vmax, APA and AP duration (APD) at 90% repolarization (APD_{90}) using LabChart 8 software

(ADInstruments). During the one-minute recording period, spontaneous AP traces without delayed afterdepolarization/early afterdepolarization (DAD/EAD) or DAD-/EAD-triggered activity or irregular beating were defined as rhythmic beating cells.

High-density multi-electrode array

According to the study protocol (Fig. 1**A**), iPSC-aCMs were cultured in RPMI/B27 medium in 6-well plates until day 30, dissociated with trypsin/EDTA, and resuspended in 2.5 µM blebbistatin buffered cardiac digestion medium. The digested cells were further filtered with a 40-µm strainer to remove large clusters and seeded onto the Geltrex-coated HD-MEA electrode distribution area (17 µg/cm^2) at a density of 1.5 million per chip. On the second day after digestion, the cardiac digestion medium was replaced with RPMI/B27 medium containing 2.5 µM blebbistatin. Starting from day 33, the culture medium was switched from RPMI/B27 to maturation medium with two-day medium changes to promote the maturation of iPSC-aCMs. On day 40, the HD-MEA containing iPSC-aCM cultures were loaded to HD-MEA in a cell culture incubator under standard cell culture conditions of 95% relative humidity, 37°C, and 5% CO_2. Recordings were performed at a 4000 Hz sampling rate (up to 50 kHz) using a highly integrated HD-MEA amplifier (Sciospec Scientific Instruments GmbH) and a self-developed program called Field Potential Recording and Analyzing Tool (FiPRAT) (*15*). iPSC-CM cultures were allowed to stabilize for 5 min before 1 min of spontaneous FP recordings were performed. For pacing and reentry induction of iPSC-aCMs, a sophisticated design of four integrated pacing electrodes (4.5 mm^2) was placed at four corners of the HD-MEA electrodes distribution area, and four independent stimulation modules were integrated into a 512-channel DAQ-system and FiPART software (*15*).

For HD-MEA data analysis, FiPART automatically processes field potential amplitudes and slopes to represent the culture by averaging over all 512 detectable electrodes during the recording time. Conduction velocity was first calculated based on the vector and a box plot was made to find the median value, and then the median values of all beats in the 1-minute recording were further averaged to represent the CV of the culture (Fig. 3**A**-**F**). Normalized amplitude and phase maps (for each time point) were processed by Hilbert transformation and further integrated into FiPART software as an analysis module as described previously in detail(*15*). Normalized field potential amplitude maps (for each time point) were integrated into the FiPART software as an analysis module. Spatial maps of activation time, representing the propagation of field potential spikes from the starting point to the end point of the electrode distribution area, were also integrated into the FiPART software.

For visualization, field potential traces from all electrodes were imported into OriginPro (OriginLab). Overlay plots were generated by superimposing all 512 traces on shared x–y axes, with color assignment indicating individual electrodes. Three-dimensional waterfall plots were constructed using the Waterfall function in OriginPro, with Z-axis representing individual electrodes. All displayed recordings represent 1-s segments of continuous data without additional filtering beyond acquisition parameters.

Western blot

On day 40, iPSC-CMs were scraped off, pelleted and snap-frozen in liquid nitrogen and stored at -80°C. Cell pellets were lysed via homogenization in RIPA buffer (150 mM NaCl, 50 mM Tris, 1.0% NP-40, 0.5% sodium deoxycholate, 0.1% SDS, 1 mM EDTA, 10 mM NaF, and 1 mM PMSF) supplemented with proteases (cOmplete mini, EDTA-free, Roche) and phosphatases (PhosSTOP, Roche) inhibitors and incubated for 30 min at 4°C with gentle rotation. Lysate was centrifuged at 20,000 × g for 20 min at 4°C and the protein concentration was determined by the BCA protein assay kit (Pierce) following the manufacturer's instructions. Proteins were subjected to SDS-PAGE and transferred to nitrocellulose membranes. Membranes were blocked with 5% non-fat milk in TBS-T at RT for 1h. Afterwards, the membranes were incubated at 4 °C overnight with primary antibodies against: Connexin 40 (Thermo Fisher Scientific, 36-4900), Nav1.5 (*SCN5A*) (1978-2016) (Alomone Labs, ASC-013), and NaK ATPase (Cell signaling technology, 3010). After TBS-T washes, membranes were incubated with anti-rabbit secondary antibody (Sigma-Aldrich, A0545) at RT for 1 h. Proteins were visualized by chemiluminescence using the SuperSignal™ West Dura Extended Duration Substrate (Thermo Fisher Scientific) or West Femto maximum sensitivity substrate (Thermo Fisher Scientific) with the Amersham ImageQuant800 (Cytiva). Images were analyzed using ImageQuant™ TL 10.2 software.

Flow cytometry

iPSC-aCMs were dissociated with trypsin/EDTA and fixed with 4% paraformaldehyde (PFA) for 20 min at room temperature and further stored in 1% BSA buffered DPBS at 4 °C. Prior to staining, iPSC-aCMs were pretreated with 0.1% Triton-X (in 1% BSA buffered DPBS solution) for 10 min at room temperature. cTnT was detected using directly coupled cTnT-APC (Miltenyi Biotec, 130-120-543). Negative controls were performed using only secondary antibodies or isotype controls (for samples detected with the directly coupled primary

antibodies). Afterwards, cells were resuspended in 1% BSA buffered DPBS and analyzed on a FACSymphony A3 (BD) flow cytometry. For all samples, 10,000 events were recorded.

Immunofluorescence staining

For immunofluorescence staining, iPSC-aCMs were dissociated and replated onto Geltrex-coated Ø25 mm glass coverslips at day 30 at a density of 2×10^5 cells per well of a 6-well plate. Cells at day 40 were fixed with methanol–acetone (7:3, v/v) for 20 min at −20 °C. Fixed cells were washed 3 times for 5 min with PBS, followed by blocking in 1% BSA (bovine serum albumin) for at least 2 h at 4 °C.

Primary antibody incubation was performed overnight at 4 °C in PBS containing 1% BSA using the following antibodies: anti-MLC2a (mouse IgG2B, Synaptic Systems, 311-011, 1:500), anti-MLC2v (rabbit IgG, Protein tech, 10906-1-AP, 1:200), anti-$Na_V1.5$ (rabbit polyclonal, Alomone Labs, ASC-013, 1:200), anti-Cx40 (rabbit-IgG, Invitrogen, 36-4900, 1:100), and anti-α-actinin (mouse IgG1, Sigma-Aldrich, A7811, 1:1000). After washing in PBS, samples were incubated with Alexa Fluor–conjugated secondary antibodies (anti-mouse Alexa Fluor 546, 1:1000, Invitrogen; anti-rabbit Alexa Fluor 488, 1:1000, Invitrogen) and Hoechst 33342 for nuclear staining for 1 h at RT. Coverslips were washed sequentially with PBS and deionized water, then mounted onto glass slides using Fluoromount-G (Thermo Fisher Scientific). Imaging was performed using a fluorescence microscope (Keyence BZ-X700E, Keyence) with a 60× oil-immersion objective.

Statistical analysis

Data are presented as the mean ± standard error of the mean (SEM). Statistical analyses were performed using GraphPad Prism 10, with different comparisons indicated in figure legends. Results were considered statistically significant when the p-value was < 0.05 (* $p < 0.05$; ** $p < 0.01$; *** $p < 0.001$; **** $p < 0.0001$).

Acknowledgments

This work was funded by the Free State of Saxony and the European Union (SAB EFRE projects “PhenoCor” with project number 100387678 to K. Guan, 100387681 to H.-G. Jahnke and “CardioEpiX” with project number 100685417 to K. Guan, 100685579 to H.-G. Jahnke.

Author Contributions

Conceptualization: WL, KG.

Methodology: WL, IC, BB, MS, XL, SS, YD, WT, MB, SW, HGJ.

Investigation: WL, IC, XL.

Visualization: WL.

Supervision: KG.

Writing—original draft: WL.

Writing—review & editing: WL, KG.

Competing interests

The authors declare no conflict of interest.

REFERENCES AND NOTES

1. J. A. Joglar, M. K. Chung, A. L. Armbruster, E. J. Benjamin, J. Y. Chyou, E. M. Cronin, A. Deswal, L. L. Eckhardt, Z. D. Goldberger, R. Gopinathannair, B. Gorenek, P. L. Hess, M. Hlatky, G. Hogan, C. Ibeh, J. H. Indik, K. Kido, F. Kusumoto, M. S. Link, K. T. Linta, G. M. Marcus, P. M. McCarthy, N. Patel, K. K. Patton, M. V. Perez, J. P. Piccini, A. M. Russo, P. Sanders, M. M. Streur, K. L. Thomas, S. Times, J. E. Tisdale, A. M. Valente, D. R. Van Wagoner, M. Peer Review Committee, 2023 ACC/AHA/ACCP/HRS Guideline for the Diagnosis and Management of Atrial Fibrillation: A Report of the American College of Cardiology/American Heart Association Joint Committee on Clinical Practice Guidelines. *Circulation* **149**, e1–e156 (2024).
2. G. Conte, M. Bergonti, V. Probst, H. Morita, J. Tfelt-Hansen, E. R. Behr, K. Kengo, E. Arbelo, L. Crotti, G. Sarquella-Brugada, A. A. M. Wilde, L. Calo, A. Sarkozy, C. de Asmundis, G. Mellor, F. Migliore, K. Letsas, A. Vicentini, M. Levinstein, P. Berne, S. A. Chen, C. Veltmann, E. K. Biernacka, P. Carvalho, M. Kabawata, K. Sojema, M. C. Gonzalez, G. Tse, A. Thollet, J. Svane, M. L. Caputo, C. Scrocco, T. Kamakura, L. F. Pardo, S. Lee, C. K. Juarez, A. Martino, L. W. Lo, C. Monaco, A. E. Reyes-Quintero, N. Martini, T. Oezkartal, C. Klersy, J. Brugada, P. J. Schwartz, P. Brugada, B. Belhassen, A. Auricchio, aTrial arrhythmias in inhEriTed aRrhythmIa Syndromes: results from the TETRIS study. *Europace* **26**, (2024).
3. M. Bergonti, G. Ciconte, J. Cruzalegui Gomez, L. Crotti, E. Arbelo, M. Casella, J. Saenen, A. Rossi, L. Pannone, E. Martinez-Barrios, P. Compagnucci, V. Russo, P. Berne, O. Van Leuven, A. Boccellino, L. Marcon, F. Dagradi, F. Landra, T. Ozkartal, A. Comune, S. Conti, V. Ribatti, O. Campuzano, P. Brugada, C. de Asmundis, J. Brugada, C. Pappone, C. Tondo, P. J. Schwartz, A. Auricchio, G. Sarquella-Brugada, G. Conte, Continuous Rhythm Monitoring With Implanted Loop Recorders in Children and Adolescents With Brugada Syndrome. *J. Am. Coll. Cardiol.* **84**, 921–933 (2024).
4. M. Bergonti, F. Sacher, E. Arbelo, L. Crotti, A. Sabbag, M. Casella, J. Saenen, A. Rossi, C. Monaco, L. Pannone, P. Compagnucci, V. Russo, E. Heller, A. Santoro, P. Berne, A. Bisignani, E. Baldi, O. Van Leuven, F. Migliore, L. Marcon, F. Dagradi, I. Sfondrini, F. Landra, A. Comune, M. Cespon-Fernandez, M. Nesti, F. Santoro, M. Magnocavallo, A. Vicentini, S. Conti, V. Ribatti, P. Brugada, C. de Asmundis, J. Brugada, C. Tondo, P. J. Schwartz, M. Haissaguerre, A. Auricchio, G. Conte, Implantable loop recorders in patients with Brugada syndrome: the BruLoop study. *Eur. Heart J.* **45**, 1255–1265 (2024).

5. J. D. Kapplinger, D. J. Tester, M. Alders, B. Benito, M. Berthet, J. Brugada, P. Brugada, V. Fressart, A. Guerchicoff, C. Harris-Kerr, S. Kamakura, F. Kyndt, T. T. Koopmann, Y. Miyamoto, R. Pfeiffer, G. D. Pollevick, V. Probst, S. Zumhagen, M. Vatta, J. A. Towbin, W. Shimizu, E. Schulze-Bahr, C. Antzelevitch, B. A. Salisbury, P. Guicheney, A. A. Wilde, R. Brugada, J. J. Schott, M. J. Ackerman, An international compendium of mutations in the SCN5A-encoded cardiac sodium channel in patients referred for Brugada syndrome genetic testing. *Heart Rhythm* **7**, 33–46 (2010).

6. A. S. Amin, G. J. Boink, F. Atrafi, A. M. Spanjaart, A. Asghari-Roodsari, R. J. Molenaar, J. M. Ruijter, A. A. Wilde, H. L. Tan, Facilitatory and inhibitory effects of SCN5A mutations on atrial fibrillation in Brugada syndrome. *Europace* **13**, 968–975 (2011).

7. W. Li, M. Stauske, X. Luo, S. Wagner, M. Vollrath, C. S. Mehnert, M. Schubert, L. Cyganek, S. Chen, S. M. Hasheminasab, G. Wulf, A. El-Armouche, L. S. Maier, G. Hasenfuss, K. Guan, Disease Phenotypes and Mechanisms of iPSC-Derived Cardiomyocytes From Brugada Syndrome Patients With a Loss-of-Function SCN5A Mutation. *Front. Cell Dev. Biol.* **8**, 592893 (2020).

8. P. R. R. van Gorp, S. A. Trines, D. A. Pijnappels, A. A. F. de Vries, Multicellular In vitro Models of Cardiac Arrhythmias: Focus on Atrial Fibrillation. *Front. Cardiovasc. Med.* **7**, 43 (2020).

9. G. E. Brown, Y. D. Han, A. R. Michell, O. T. Ly, C. G. Vanoye, E. Spanghero, A. L. George, Jr., D. Darbar, S. R. Khetani, Engineered cocultures of iPSC-derived atrial cardiomyocytes and atrial fibroblasts for modeling atrial fibrillation. *Sci. Adv.* **10**, eadg1222 (2024).

10. P. Benzoni, G. Campostrini, S. Landi, V. Bertini, E. Marchina, M. Iascone, G. Ahlberg, M. S. Olesen, E. Crescini, C. Mora, G. Bisleri, C. Muneretto, R. Ronca, M. Presta, P. L. Poliani, G. Piovani, R. Verardi, E. Di Pasquale, A. Consiglio, A. Raya, E. Torre, A. M. Lodrini, R. Milanesi, M. Rocchetti, M. Baruscotti, D. DiFrancesco, M. Memo, A. Barbuti, P. Dell'Era, Human iPSC modelling of a familial form of atrial fibrillation reveals a gain of function of If and ICaL in patient-derived cardiomyocytes. *Cardiovasc. Res.* **116**, 1147–1160 (2020).

11. M. Pierre, M. Djemai, V. Pouliot, H. Poulin, M. H. Gollob, M. Chahine, Exploring SCN5A variants associated with atrial fibrillation in atrial cardiomyocytes derived from human induced pluripotent stem cells: A characterization study. *Heart Rhythm* **22**, 1574–1587 (2025).

12. L. Hong, M. Zhang, O. T. Ly, H. Chen, A. Sridhar, E. Lambers, B. Chalazan, S. W. Youn, M. Maienschein-Cline, L. Feferman, S. G. Ong, J. C. Wu, J. Rehman, D. Darbar, Human induced pluripotent stem cell-derived atrial cardiomyocytes carrying an SCN5A mutation identify nitric oxide signaling as a mediator of atrial fibrillation. *Stem Cell Reports* **16**, 1542–1554 (2021).

13. N. Harlaar, S. O. Dekker, J. Zhang, R. R. Snabel, M. W. Veldkamp, A. O. Verkerk, C. C. Fabres, V. Schwach, L. J. S. Lerink, M. R. Rivaud, A. A. Mulder, W. E. Corver, M. Goumans, D. Dobrev, R. J. M. Klautz, M. J. Schalij, G. J. C. Veenstra, R. Passier, T. J. van Brakel, D. A. Pijnappels, A. A. F. de Vries, Conditional immortalization of human atrial myocytes for the generation of in vitro models of atrial fibrillation. *Nat Biomed Eng* **6**, 389–402 (2022).

14. N. Shaheen, A. Shiti, I. Huber, R. Shinnawi, G. Arbel, A. Gepstein, N. Setter, I. Goldfracht, A. Gruber, S. V. Chorna, L. Gepstein, Human Induced Pluripotent Stem Cell-Derived Cardiac Cell Sheets Expressing Genetically Encoded Voltage Indicator for Pharmacological and Arrhythmia Studies. *Stem Cell Reports* **10**, 1879–1894 (2018).

15. S. Schmidt, W. Li, M. Schubert, B. Binnewerg, C. Pronnecke, F. D. Zitzmann, M. Bulst, S. Wegner, M. Meier, K. Guan, H. G. Jahnke, Novel high-dense microelectrode array based multimodal bioelectronic monitoring system for cardiac arrhythmia re-entry analysis. *Biosens Bioelectron* **252**, 116120 (2024).
16. E. Schulze-Bahr, L. Eckardt, G. Breithardt, K. Seidl, T. Wichter, C. Wolpert, M. Borggrefe, W. Haverkamp, Sodium channel gene (SCN5A) mutations in 44 index patients with Brugada syndrome: different incidences in familial and sporadic disease. *Hum Mutat* **21**, 651–652 (2003).
17. C. C. Veerman, I. Mengarelli, K. Guan, M. Stauske, J. Barc, H. L. Tan, A. A. Wilde, A. O. Verkerk, C. R. Bezzina, hiPSC-derived cardiomyocytes from Brugada Syndrome patients without identified mutations do not exhibit clear cellular electrophysiological abnormalities. *Sci. Rep.* **6**, 30967 (2016).
18. W. Li, X. Luo, A. Strano, S. Arun, O. Gamm, M. S. Poetsch, M. Hasse, R. P. Steiner, K. Fischer, J. Poche, Y. Ulbricht, M. Lesche, G. Trimaglio, A. El-Armouche, A. Dahl, P. Mirtschink, K. Guan, M. Schubert, Comprehensive promotion of iPSC-CM maturation by integrating metabolic medium with nanopatterning and electrostimulation. *Nat. Commun.* **16**, 2785 (2025).
19. L. Cyganek, M. Tiburcy, K. Sekeres, K. Gerstenberg, H. Bohnenberger, C. Lenz, S. Henze, M. Stauske, G. Salinas, W. H. Zimmermann, G. Hasenfuss, K. Guan, Deep phenotyping of human induced pluripotent stem cell-derived atrial and ventricular cardiomyocytes. *JCI insight* **3**, (2018).
20. D. Malan, S. Friedrichs, B. K. Fleischmann, P. Sasse, Cardiomyocytes obtained from induced pluripotent stem cells with long-QT syndrome 3 recapitulate typical disease-specific features in vitro. *Circulation research* **109**, 841–847 (2011).
21. R. P. Davis, S. Casini, C. W. van den Berg, M. Hoekstra, C. A. Remme, C. Dambrot, D. Salvatori, D. W. Oostwaard, A. A. Wilde, C. R. Bezzina, A. O. Verkerk, C. Freund, C. L. Mummery, Cardiomyocytes derived from pluripotent stem cells recapitulate electrophysiological characteristics of an overlap syndrome of cardiac sodium channel disease. *Circulation* **125**, 3079–3091 (2012).
22. N. J. Severs, A. F. Bruce, E. Dupont, S. Rothery, Remodelling of gap junctions and connexin expression in diseased myocardium. *Cardiovasc. Res.* **80**, 9–19 (2008).
23. S. Nattel, J. Heijman, L. Zhou, D. Dobrev, Molecular Basis of Atrial Fibrillation Pathophysiology and Therapy: A Translational Perspective. *Circulation research* **127**, 51–72 (2020).
24. G. Y. Lip, L. Fauchier, S. B. Freedman, I. Van Gelder, A. Natale, C. Gianni, S. Nattel, T. Potpara, M. Rienstra, H. F. Tse, D. A. Lane, Atrial fibrillation. *Nat Rev Dis Primers* **2**, 16016 (2016).
25. S. Nattel, D. Dobrev, Controversies About Atrial Fibrillation Mechanisms: Aiming for Order in Chaos and Whether it Matters. *Circulation research* **120**, 1396–1398 (2017).
26. J. Heijman, N. Voigt, S. Nattel, D. Dobrev, Cellular and molecular electrophysiology of atrial fibrillation initiation, maintenance, and progression. *Circulation research* **114**, 1483–1499 (2014).
27. R. Wakili, N. Voigt, S. Kaab, D. Dobrev, S. Nattel, Recent advances in the molecular pathophysiology of atrial fibrillation. *J. Clin. Invest.* **121**, 2955–2968 (2011).
28. G. Sarquella-Brugada, O. Campuzano, E. Arbelo, J. Brugada, R. Brugada, Brugada syndrome: clinical and genetic findings. *Genet Med* **18**, 3–12 (2016).
29. A. Owais, M. Barney, O. T. Ly, G. Brown, H. Chen, A. Sridhar, A. Pavel, S. R. Khetani, D. Darbar, Genetics and Pharmacogenetics of Atrial Fibrillation: A Mechanistic Perspective. *JACC Basic Transl Sci* **9**, 918–934 (2024).

30. M. E. Sweat, W. T. Pu, Genetic and Molecular Underpinnings of Atrial Fibrillation. *NPJ Cardiovasc Health* **1**, (2024).
31. P. Sanders, O. Berenfeld, M. Hocini, P. Jais, R. Vaidyanathan, L. F. Hsu, S. Garrigue, Y. Takahashi, M. Rotter, F. Sacher, C. Scavee, R. Ploutz-Snyder, J. Jalife, M. Haissaguerre, Spectral analysis identifies sites of high-frequency activity maintaining atrial fibrillation in humans. *Circulation* **112**, 789–797 (2005).
32. Z. Laksman, M. Wauchop, E. Lin, S. Protze, J. Lee, W. Yang, F. Izaddoustdar, S. Shafaattalab, L. Gepstein, G. F. Tibbits, G. Keller, P. H. Backx, Modeling Atrial Fibrillation using Human Embryonic Stem Cell-Derived Atrial Tissue. *Sci. Rep.* **7**, 5268 (2017).
33. H. Pohjantahti-Maaroos, H. Hyppola, M. Lekkala, E. Sinisalo, A. Heikkola, J. Hartikainen, Intravenous vernakalant in comparison with intravenous flecainide in the cardioversion of recent-onset atrial fibrillation. *Eur Heart J Acute Cardiovasc Care* **8**, 114–120 (2019).
34. G. N. Beatch, B. Mangal, Safety and efficacy of vernakalant for the conversion of atrial fibrillation to sinus rhythm; a phase 3b randomized controlled trial. *BMC Cardiovasc Disord* **16**, 113 (2016).
35. H. Crijns, A. Elvan, N. Al-Windy, Y. S. Tuininga, E. Badings, I. Aksoy, I. C. Van Gelder, P. Madhavapeddi, A. J. Camm, P. R. Kowey, J. N. Ruskin, L. Belardinelli, I. Investigators*, Open-Label, Multicenter Study of Flecainide Acetate Oral Inhalation Solution for Acute Conversion of Recent-Onset, Symptomatic Atrial Fibrillation to Sinus Rhythm. *Circ Arrhythm Electrophysiol* **15**, e010204 (2022).
36. E. Wettwer, T. Christ, S. Endig, N. Rozmaritsa, K. Matschke, J. J. Lynch, M. Pourrier, J. K. Gibson, D. Fedida, M. Knaut, U. Ravens, The new antiarrhythmic drug vernakalant: ex vivo study of human atrial tissue from sinus rhythm and chronic atrial fibrillation. *Cardiovasc Res* **98**, 145–154 (2013).
37. A. J. Camm, G. V. Naccarelli, S. Mittal, H. Crijns, S. H. Hohnloser, C. S. Ma, A. Natale, M. P. Turakhia, P. Kirchhof, The Increasing Role of Rhythm Control in Patients With Atrial Fibrillation: JACC State-of-the-Art Review. *J. Am. Coll. Cardiol.* **79**, 1932–1948 (2022).
38. K. Streckfuss-Bomeke, F. Wolf, A. Azizian, M. Stauske, M. Tiburcy, S. Wagner, D. Hubscher, R. Dressel, S. Chen, J. Jende, G. Wulf, V. Lorenz, M. P. Schon, L. S. Maier, W. H. Zimmermann, G. Hasenfuss, K. Guan, Comparative study of human-induced pluripotent stem cells derived from bone marrow cells, hair keratinocytes, and skin fibroblasts. *Eur. Heart J.* **34**, 2618–2629 (2013).
39. U. Rossler, A. F. Hennig, N. Stelzer, S. Bose, J. Kopp, K. Soe, L. Cyganek, G. Zifarelli, S. Ali, M. von der Hagen, E. T. Strassler, G. Hahn, M. Pusch, T. Stauber, Z. Izsvak, M. Gossen, H. Stachelscheid, U. Kornak, Efficient generation of osteoclasts from human induced pluripotent stem cells and functional investigations of lethal CLCN7-related osteopetrosis. *J Bone Miner Res* **36**, 1621–1635 (2021).
40. W. Li, X. Luo, Y. Ulbricht, M. Wagner, C. Piorkowski, A. El-Armouche, K. Guan, Establishment of an automated patch-clamp platform for electrophysiological and pharmacological evaluation of hiPSC-CMs. *Stem Cell Res.* **41**, 101662 (2019).
41. W. Li, X. Luo, Y. Ulbricht, K. Guan, Blebbistatin protects iPSC-CMs from hypercontraction and facilitates automated patch-clamp based electrophysiological study. *Stem Cell Res.* **56**, 102565 (2021).
42. X. Luo, W. Li, K. Kunzel, S. Henze, L. Cyganek, A. Strano, M. S. Poetsch, M. Schubert, K. Guan, IP3R-Mediated Compensatory Mechanism for Calcium Handling in Human Induced Pluripotent Stem Cell-Derived Cardiomyocytes With Cardiac Ryanodine Receptor Deficiency. *Front. Cell Dev. Biol.* **8**, 772 (2020).

931

932

933

934